Electronic Supplementary Material (ESI) for Journal of Materials Chemistry A.

Supplementary Information

In situ oxidation transformation of trimetallic selenide to amorphous FeCo-oxyhydroxide by self-sacrificing $MoSe_2$ for efficient water oxidation

Yu-Jia Tang, [a] Yu Wang, [b] and Kun Zhou, [a,b,*]

[a] School of Mechanical and Aerospace Engineering, Nanyang Technological University, 50 Nanyang Avenue, Singapore 639798, Singapore

[b] Environmental Process Modelling Centre, Nanyang Environment and Water Research Institute, Nanyang Technological University, 1 CleanTech Loop, Singapore 637141, Singapore

* Corresponding author

E-mail: kzhou@ntu.edu.sg

Computational details:

The modelling results were obtained at the density functional theory plus Hubbard-U (DFT + U) level, as implemented in Vienna *ab* Initio Simulation package (VASP) code.[1,2] The revised Perdew–Burke–Ernzerhof exchange-correlation functional[3] and projector-augmented wave approach[4,5] were employed. Spin polarization was included in all calculations with a smearing width of 0.1 eV within the Gaussian scheme. We applied the Hubbard-U approach introduced by Dudarev and co-workers,[6] and the effective Hubbard-U parameter (*U-J*) was set as 3.52 eV for Co and 3.50 eV for Fe.[7] The cutoff energy was 400 eV and the *k*-point sampling was 5 × 3 × 1. The convergence threshold of energy was 1×10^{-5} eV, and that of force on each ion was 0.02 eV $Å^{-1}$. The vacuum space of slabs was kept being larger than 15 Å to keep the image interaction negligible, and the dipole correction was included in slab calculations.

The alkaline OER process typically involves the following steps:

$$* + OH^- \rightarrow OH^* + e^- \quad (1)$$

$$OH + OH^- \rightarrow O^* + H_2O + e^- \quad (2)$$

$$O^* + OH^- \rightarrow OOH^* + e^- \quad (3)$$

$$OOH^* + OH^- \rightarrow O_2 + H_2O + e^- + * \quad (4)$$

where * denotes an adsorption site. OH*, O* and OOH* are the OER intermediates. The adsorption free energies to OH* (ΔG_{OH^*}), O* (ΔG_{O^*}), and OOH* (ΔG_{OOH^*}) are calculated as follows:

$$\Delta G_{OH^*} = G_{OH^*} - G_* - (G_{H2O} - 1/2G_{H2}) \quad (5)$$

$$\Delta G_{O^*} = G_{O^*} - G_* - (G_{H2O} - G_{H2}) \quad (6)$$

$$\Delta G_{OOH^*} = G_{OOH^*} - G_* - (2G_{H2O} - 3/2G_{H2}) \quad (7)$$

where *G* is the free energy of the given species, which can be deduced from the zero-point energy (E_{ZPE}) and entropy (*TS*) corrections to the DFT energy of species (E_{DFT}). The E_{ZPE} and *S* of adsorbates are obtained by vibrational frequencies calculations with using harmonic vibrational motions and neglecting contributions from slab, whereas for H_2O and H_2 molecules, these are taken from the NIST database (http://cccbdb.nist.gov/). These correction values are summarized in Table S3. The free energy change for the above four OER steps (eqs. 1–4) can be derived as follows:

$$\Delta G_1 = \Delta G_{OH^*} - eU + G_{pH} \quad (8)$$

$$\Delta G_2 = \Delta G_{O^*} - \Delta G_{OH^*} - eU + G_{pH} \quad (9)$$

$$\Delta G_3 = \Delta G_{OOH^*} - \Delta G_{O^*} - eU + G_{pH} \quad (10)$$

$$\Delta G_4 = 4.92 - \Delta G_{OOH^*} - eU + G_{pH} \quad (11)$$

where *U* is the electrode potential and G_{pH} is the contribution of pH derived by $G_{pH} = -k_B T \ln(10) \times pH$, according to the CHE model. Specially, the step that has the largest Δ*G* value among the four Δ*G* values represents the potential-limiting step. Then the theoretical overpotentials (η^t) of OER can be calculated using the equation:

$$\eta^{t} = \max\{\Delta G_1, \Delta G_2, \Delta G_3, \Delta G_4\}/e - 1.23\ V \quad (12)$$

Note that the calculated η^{t} is only a thermodynamic quantity, but it has been found to scale well with experimentally measured overpotential.[8]

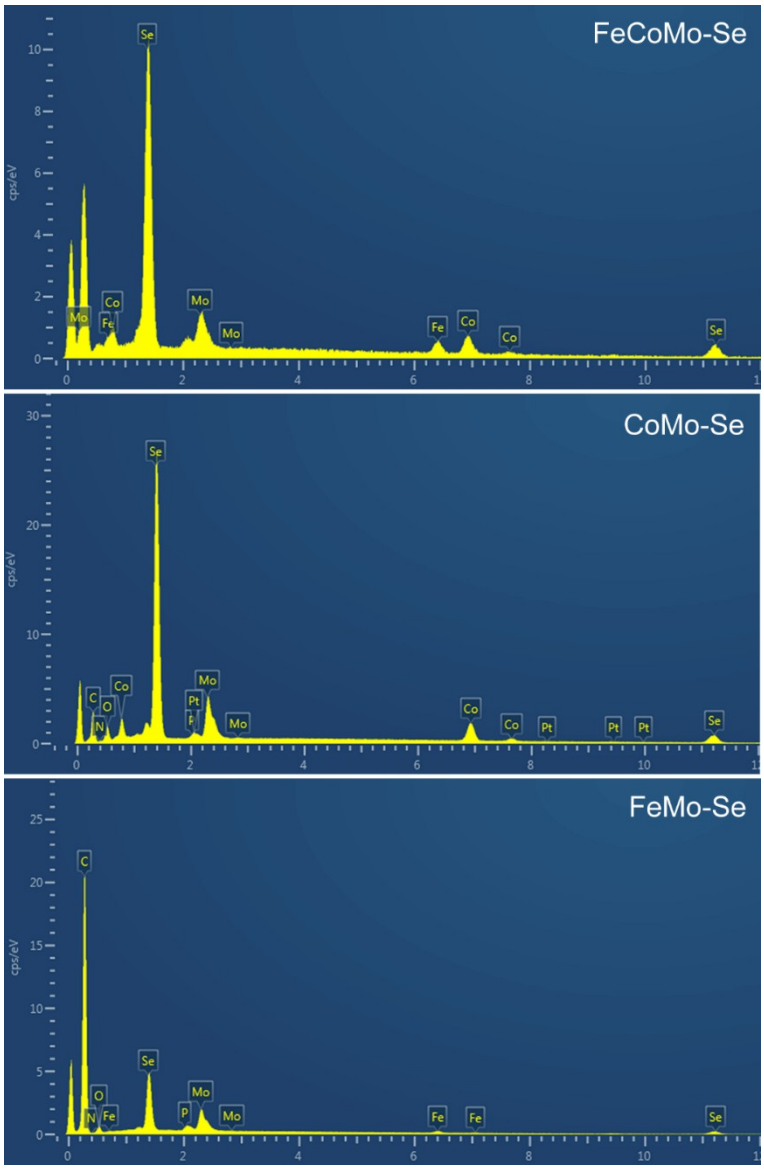

Figure S1. EDX spectra of the as-prepared selenide samples of FeCoMo-Se, CoMo-Se and FeMo-Se.

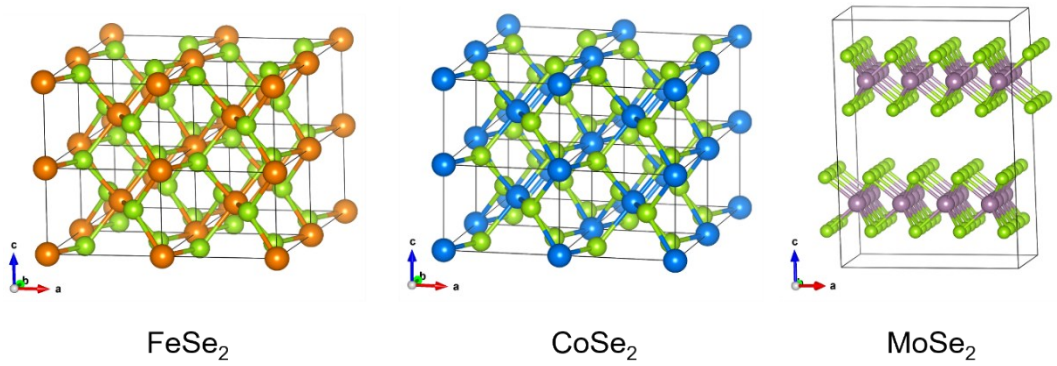

Figure S2. Geometric structures of $FeSe_2$, $CoSe_2$ and $MoSe_2$, where Fe, Co, Mo, and Se are represented by orange, blue, purple and green balls, respectively.

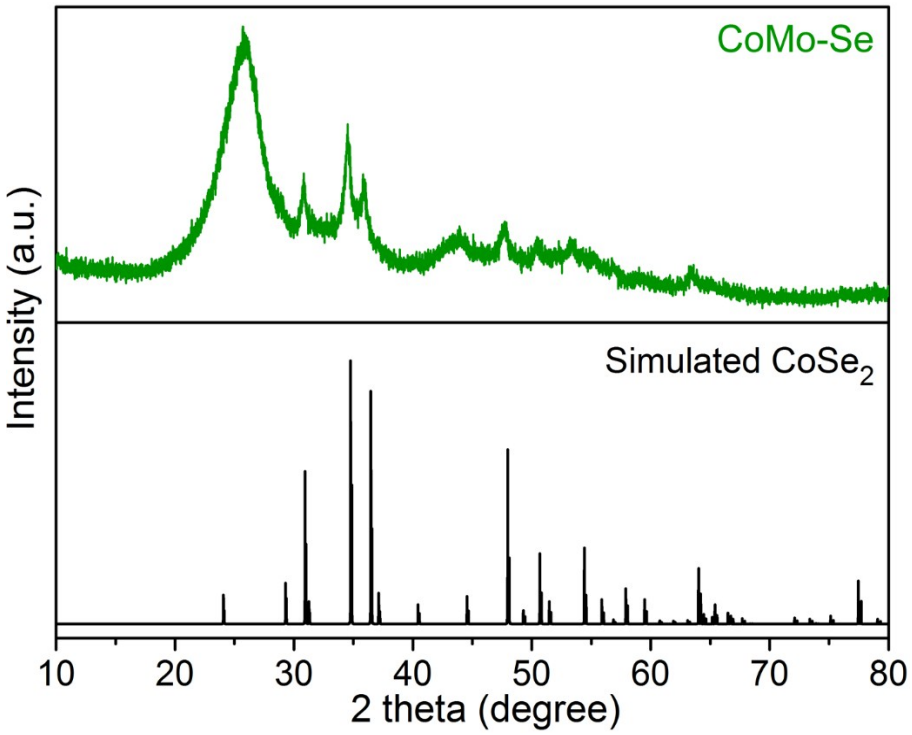

Figure S3. PXRD pattern of CoMo-Se and the simulated one of $CoSe_2$.

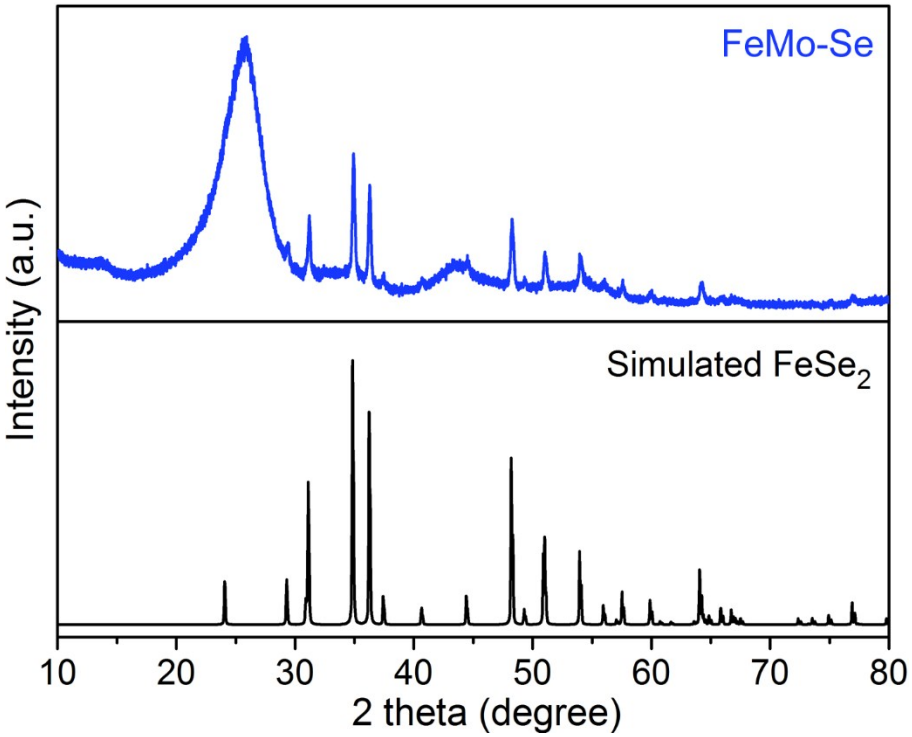

Figure S4. PXRD pattern of FeMo-Se and the simulated one of $FeSe_2$.

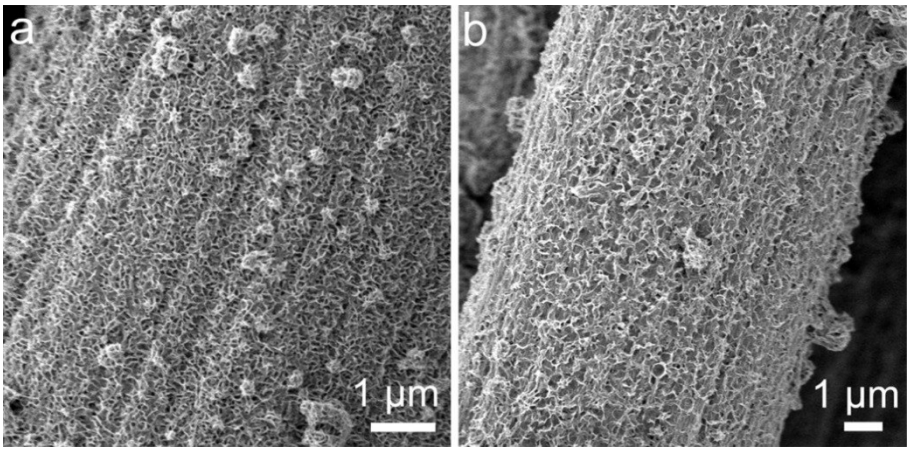

Figure S5. SEM images of (a) CoMo-Se and (b) FeMo-Se.

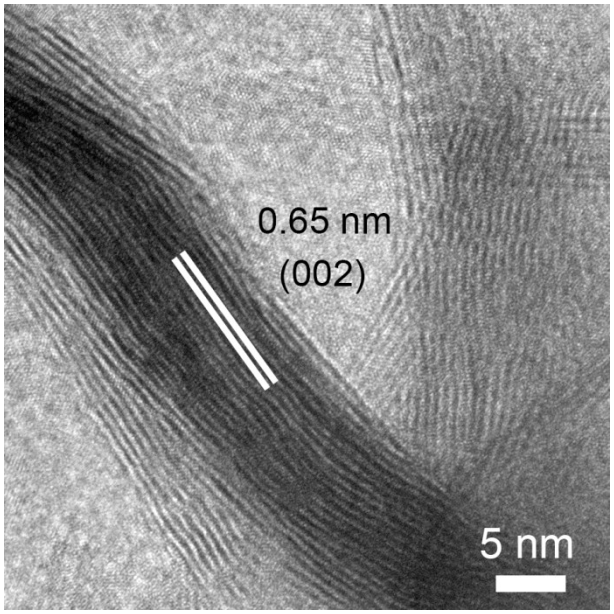

Figure S6. HRTEM image of $MoSe_2$ ultrasonicated from the CC substrate.

$MoSe_2$ on the CC substrate was synthesized using a similar hydrothermal method without adding $Co(NO_3)_2{\cdot}6H_2O$ and $FeCl_3$. HRTEM image shows that $MoSe_2$ possesses a multilayer structure with an interplanar distance of 0.65 nm for the (002) plane, which is in accordance with the pristine $MoSe_2$.

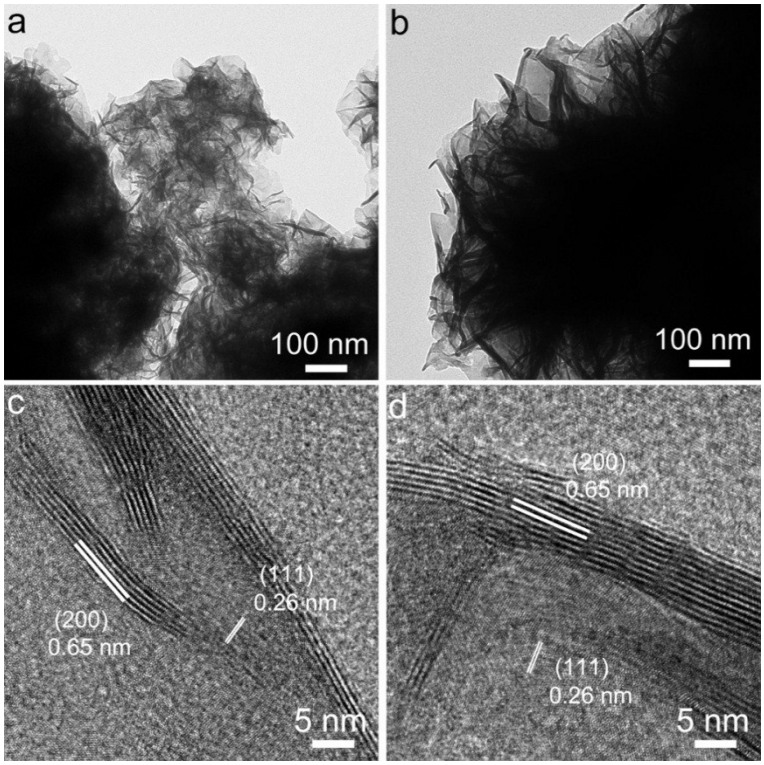

Figure S7. TEM images of (a) CoMo-Se and (b) FeMo-Se ultrasonicated from the CC substrate. HRTEM images of (c) CoMo-Se and (d) FeMo-Se ultrasonicated from the CC substrate.

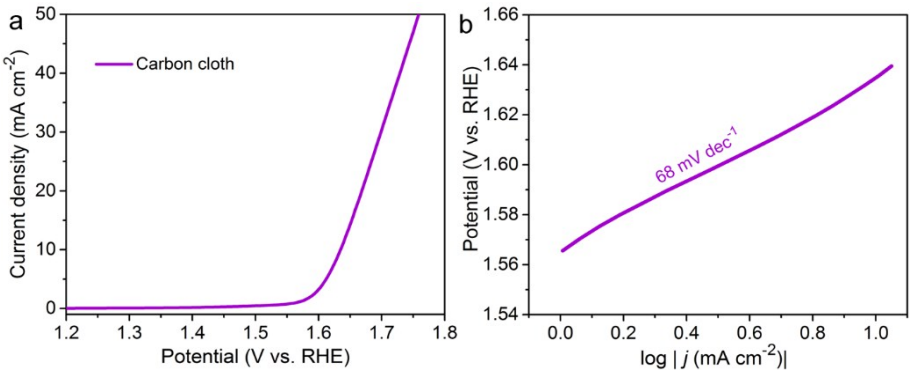

Figure S8. Electrochemical activity of the treated carbon cloth substrate for OER: (a) LSV curve and (b) Tafel plot.

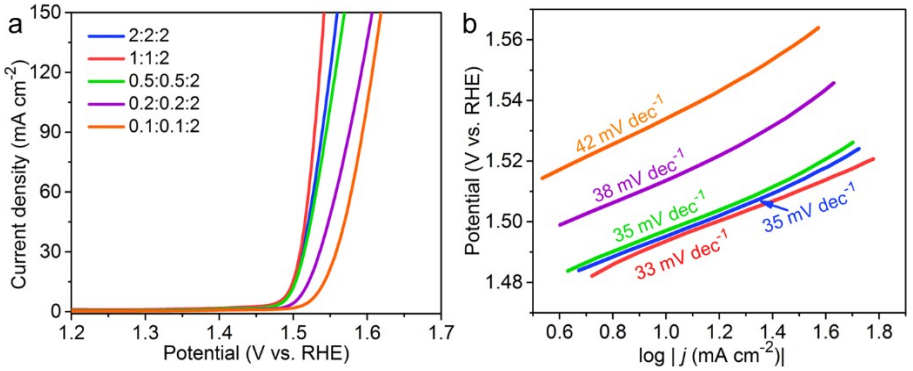

Figure S9. Electrochemical activity of the trimetallic selenides synthesized with different molar ratios of Fe, Co and Mo in precursors for OER: (a) LSV curves and (b) Tafel plots.

Different mol ratios of Fe, Co and Mo in the precursors, *i.e.*, 2:2:2, 1:1:2, 0.5:0.5:2, 0.2:0.2:2 and 0.1:0.1:2, were chosen to select the optimum synthesis condition for the trimetallic selenides. According to the LSV curves and Tafel slopes, the trimetallic selenide with the mol ratio of 1:1:2 in the precursor had the best OER performance among all the as-prepared $MoSe_2$-containing trimetallic selenide catalysts.

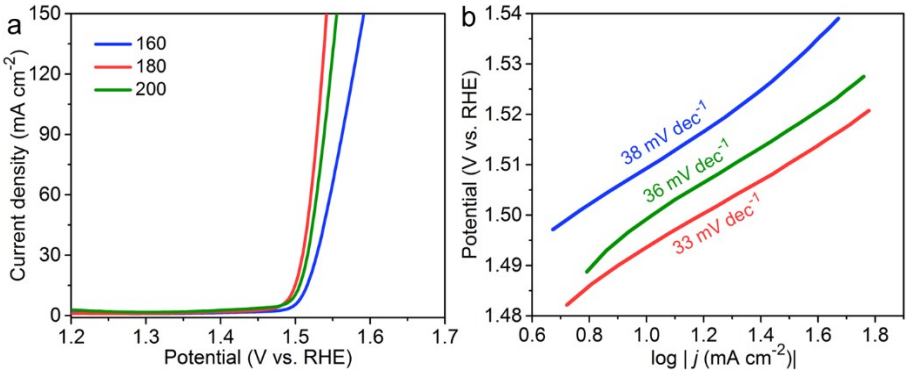

Figure S10. Electrochemical activity of the trimetallic selenides synthesized at different hydrothermal temperatures (160, 180 and 200 °C) for OER: (a) LSV curves and (b) Tafel plots.

The trimetallic selenides were prepared by adjusting the hydrothermal temperatures (160, 180 and 200 °C). The trimetallic selenide prepared at 180 °C showed the lowest η_{10} and Tafel slope among all the selenide samples.

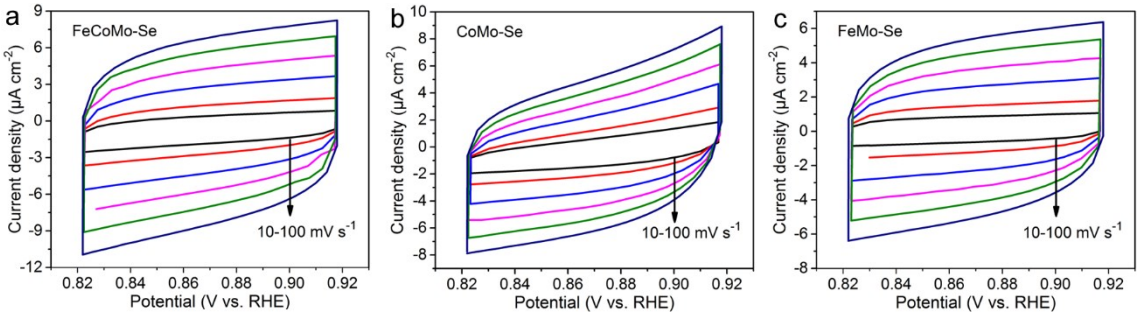

Figure S11. CV curves of (a) FeCoMo-Se, (b) CoMo-Se and (c) FeMo-Se loaded onto GCE obtained in a potential range from 0.82 to 0.92 V *vs.* RHE at the different scan rates (10, 20, 40, 60, 80 and 100 mV s^{-1}).

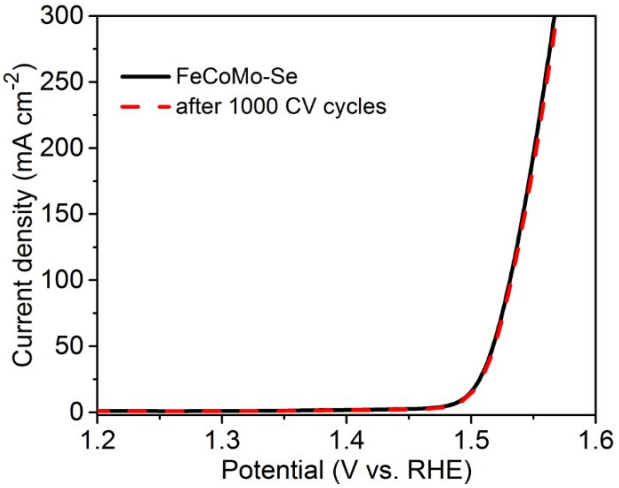

Figure S12. LSV curves of FeCoMo-Se before and after 1000 CV cycles stability testing for OER.

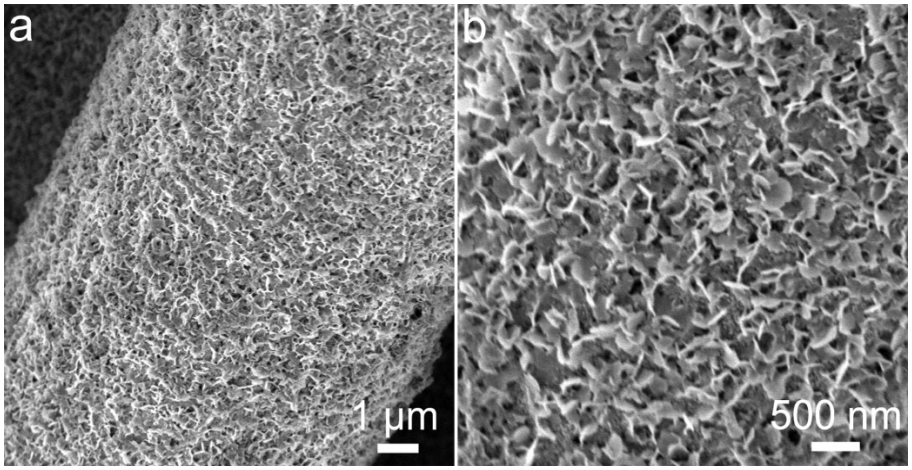

Figure S13. Low- and high-magnification SEM images of FeCoMo-Se after 1000 CV cycles stability testing in 1 M KOH for OER.

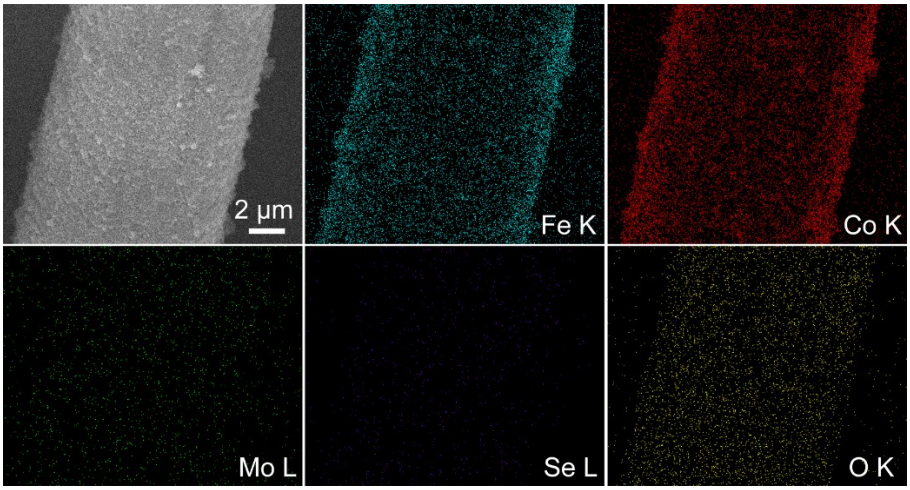

Figure S14. EDX element mapping images of Fe, Co, Mo, Se and O of FeCoMo-Se after 1000 CV cycles stability testing in 1 M KOH for OER.

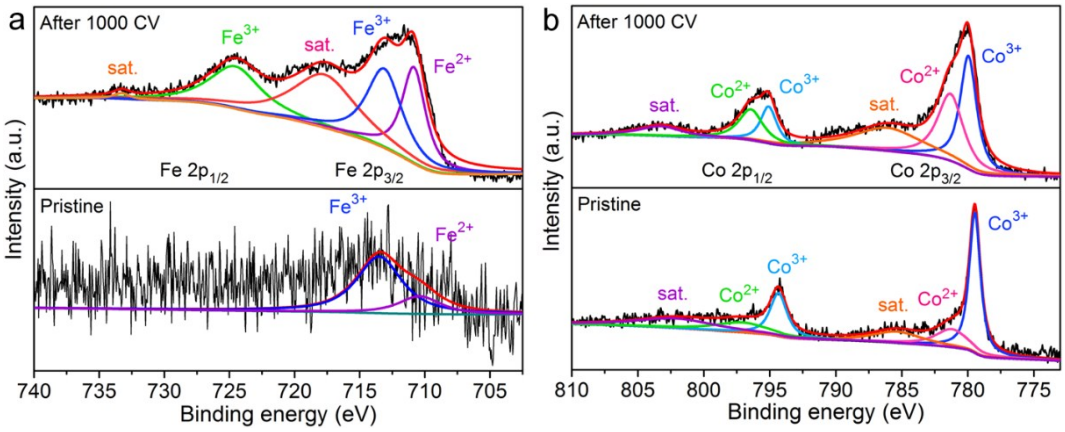

Figure S15. High-resolution XPS spectra of FeCoMo-Se before and after stability testing in 1 M KOH for OER: (a) Fe 2p and (b) Co 2p.

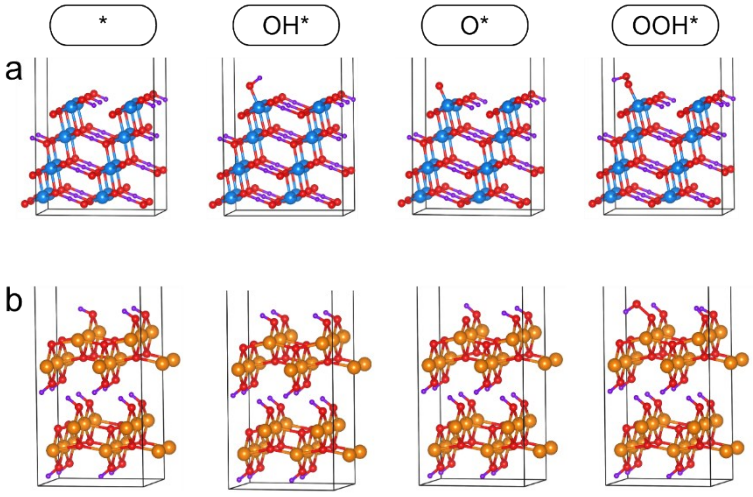

Figure S16. Optimized structures of intermediates for OER on (a) Co-oxyhydroxide and (b) Fe-oxyhydroxide. Co, Fe, O, and H are represented by blue, orange, red, and purple balls, respectively.

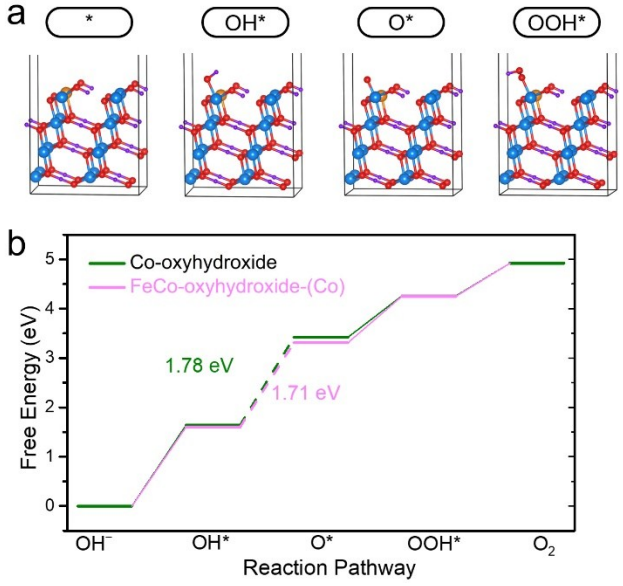

Figure S17. (a) Optimized structures of intermediates of OER on the Co site of FeCo-oxyhydroxide and (b) the free energy diagram for OER on the Co sites of FeCo-oxyhydroxide and pristine Co-oxyhydroxide. The dashed lines denote the potential-limiting steps. The numbers represent the values of free energy change of the potential-limiting steps.

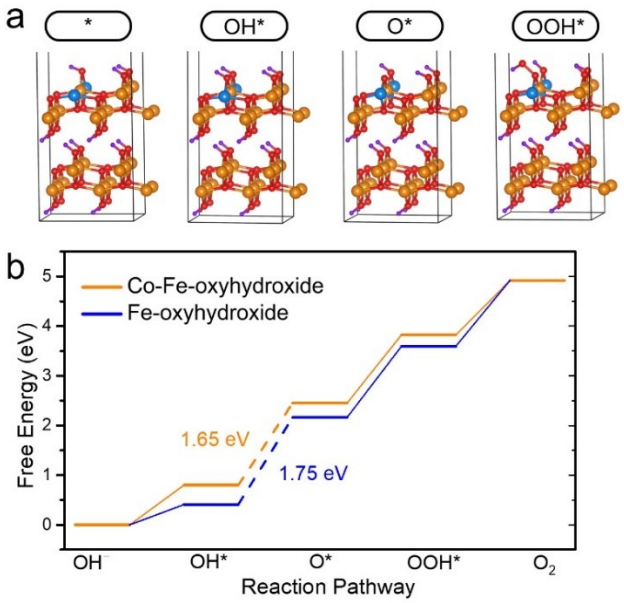

Figure S18. (a) Optimized structures of intermediates of Co-Fe-oxyhydroxide and (b) the free energy diagram for OER on Co-Fe-oxyhydroxide and pristine Fe-oxyhydroxide. Co-Fe-oxyhydroxide was constructed by introducing a Co dopant into Fe-oxyhydroxide. The dashed lines denote the potential-limiting steps. The numbers represent the values of free energy change of the potential-limiting steps. It was found that Co-Fe-oxyhydroxide (1.65 eV) and Fe-oxyhydroxide (1.75 eV) have the same potential-limiting step, O* formation step, and Co-Fe-oxyhydroxide exhibits higher OER activity than Fe-oxyhydroxide.

Table S1. Comparison of OER performances of FeCoMo-Se and recently reported transition-metal-based selenide and (oxy)hydroxide electrocatalysts.

Electrocatalyst	Substrate	Electrolyte	η_{10} (mV)	Tafel Slope (mV dec^{-1})	Reference
FeCoMo-Se	**Carbon cloth**	**1 M KOH**	**264**	**33**	**This work**
$Ni_xFe_{1-x}Se_2$-DO	Ni foam	1 M KOH	195	28	[9]
ECT-Se-$Co_{0.37}Ni_{0.26}Fe_{0.37}O$	Carbon fiber cloth	1 M KOH	243	35.1	[10]
$(Ni,Co)Se_2$	Carbon cloth	1 M KOH	256	74	[11]
NiFe-LDH	Glassy carbon	1 M KOH	270	36.2	[12]
$(Co_{0.21}Ni_{0.25}Cu_{0.54})_3Se_2$	Au-coated glass substrate	1 M KOH	272	53.5	[13]
Mo intercalated NiFe LDH	Glassy carbon	1 M KOH	280	40	[14]
Ni-Fe LDH	Glassy carbon	1 M KOH	280	49.4	[15]

$Co(S_{0.22}Se_{0.78})_2$	Ni foam	1 M KOH	283	65.6	[16]
FeOOH(Se)	Iron foam	1 M KOH	287	54	[17]
α-$Co_4Fe(OH)_x$	Glassy carbon	1 M KOH	295	52	[18]
CoZn-Se	Glassy carbon	1 M KOH	320	66	[19]
Fe-CoOOH/G	Glassy carbon	1 M KOH	330	37	[20]

Table S2. Calculated adsorption free energies of intermediates of the studied systems.

	Co-oxyhydroxide	FeCo-oxyhydroxide (Co site)	Fe-oxyhydroxide	Co-Fe-oxyhydroxide	FeCo-oxyhydroxide (Fe site)
ΔG_{OH*} (eV)	1.64	1.60	0.41	0.80	1.52
ΔG_{O*} (eV)	3.42	3.31	2.16	2.45	2.92
ΔG_{OOH*}(eV)	4.26	4.26	3.59	3.82	4.16

Table S3. Calculated zero-pint energy correction (E_{ZPE}), entropy contribution (TS), and the total free energy correction ($G - E_{DFT}$) of the studied systems.

Species	E_{ZPE}	−TS	$G - E_{DFT}$
H_2	0.27	−0.40	−0.13
H_2O	0.56	−0.67	−0.11
OH* on Co-oxyhydroxide	0.35	−0.10	0.25
OH* on Fe-oxyhydroxide	0.37	−0.07	0.30
OH* on FeCo-oxyhydroxide	0.35	−0.10	0.25
O* on Co-oxyhydroxide	0.07	−0.05	0.02
O* on Fe-oxyhydroxide	0.07	−0.04	0.03
O* on FeCo-oxyhydroxide	0.08	−0.05	0.03
OOH* on Co-oxyhydroxide	0.47	−0.14	0.33
OOH* on Fe-oxyhydroxide	0.46	−0.14	0.32
OOH* on FeCo-oxyhydroxide	0.46	−0.14	0.32

References

1 G. Kresse and J. Hafner, *Phys. Rev. B*, 1993, **47**, 558.

2 G. Kresse and J. Furthmüller, *Comp. Mate. Sci.*, 1996, **6**, 15-50.

3 B. Hammer, L. B. Hansen and J. K. Nørskov, *Phys. Rev. B*, 1999, **59**, 7413.

4 P. E. Blöchl, *Phys. Rev. B*, 1994, **50**, 17953.

5 G. Kresse and D. Joubert, *Phys. Rev. B*, 1999, **59**, 1758.

6 S. Dudarev, G. Botton, S. Savrasov, C. Humphreys and A. Sutton, *Phys. Rev. B*, 1998, **57**, 1505.

7 M. García-Mota, M. Bajdich, V. Viswanathan, A. Vojvodic, A. T. Bell and J. K. Nørskov, *J. Phys. Chem. C*, 2012, **116**, 21077-21082.

8 I. C. Man, H. Y. Su, F. Calle-Vallejo, H. A. Hansen, J. I. Martínez, N. G. Inoglu, J. Kitchin, T. F. Jaramillo, J. K. Nørskov and J. Rossmeisl, *ChemCatChem*, 2011, **3**, 1159-1165.

9 X. Xu, F. Song and X. Hu, *Nat. Commun.*, 2016, **7**, 12324.

10 W. Chen, Y. Liu, Y. Li, J. Sun, Y. Qiu, C. Liu, G. Zhou and Y. Cui, *Nano Lett.*, 2016, **16**, 7588-7596.

11 W. Song, X. Teng, Y. Liu, J. Wang, Y. Niu, X. He, C. Zhang and Z. Chen, *Nanoscale*, 2019, **11**, 6401-6409.

12 D. Zhou, S. Wang, Y. Jia, X. Xiong, H. Yang, S. Liu, J. Tang, J. Zhang, D. Liu, L. Zheng, Y. Kuang, X. Sun and B. Liu, *Angew. Chem. Int. Ed.*, 2019, **131**, 746-750.

13 X. Cao, E. Johnson and M. Nath, *J. Mater. Chem. A*, 2019, **7**, 9877-9889.

14 N. Han, F. Zhao and Y. Li, *J. Mater. Chem. A*, 2015, **3**, 16348-16353.

15 L. Yu, J. F. Yang, B. Y. Guan, Y. Lu and X. W. Lou, *Angew. Chem. Int. Ed.*, 2018, **57**, 172-176.

16 L. Fang, W. Li, Y. Guan, Y. Feng, H. Zhang, S. Wang and Y. Wang, *Adv. Funct. Mater.*, 2017, **27**, 1701008.

17 S. Niu, W.-J. Jiang, Z. Wei, T. Tang, J. Ma, J.-S. Hu and L.-J. Wan, *J. Am. Chem. Soc.*, 2019, **141**, 7005-7013.

18 H. Jin, S. Mao, G. Zhan, F. Xu, X. Bao and Y. Wang, *J. Mater. Chem. A*, 2017, **5**, 1078-1084.

19 G. Fang, Q. Wang, J. Zhou, Y. Lei, Z. Chen, Z. Wang, A. Pan and S. Liang, *ACS Nano*, 2019, **13**, 5635-5645.

20 X. Han, C. Yu, S. Zhou, C. Zhao, H. Huang, J. Yang, Z. Liu, J. Zhao and J. Qiu, *Adv. Energy Mater.*, 2017, **7**, 1602148.